

1 **Title: Local distribution of collagen fibers determines crack initiation site and its**
2 **propagation direction during aortic rupture**

3
4 Shukei Sugita and Takeo Matsumoto*, *Nagoya, Japan*

5
6 **Affiliation and address:**

7 Biomechanics Laboratory, Department of Mechanical Engineering, Graduate School of
8 Engineering, Nagoya Institute of Technology, Gokiso-cho, Showa-ku, Nagoya 466-8555,
9 JAPAN

10 *Current: Department of Mechanical Systems Engineering, Graduate School of Engineering,
11 Nagoya University, Furo-cho, Chikusa-ku, Nagoya 464-8603, JAPAN

12
13
14 **To whom correspondence should be addressed:**

15 Shukei Sugita, Ph.D.

16 Department of Mechanical Engineering, Graduate School of Engineering, Nagoya Institute
17 of Technology

18 Gokiso-cho, Showa-ku, Nagoya 466-8555, JAPAN

19 Tel. and Fax: +81 52 735 7125

20 E-mail: sugita.shukei@nitech.ac.jp

21
22 **Acknowledgments**

23 This work was supported in part by Japan Society for the Promotion of Science KAKENHI
24 (Nos. 26709002 and 15H02209) and AMED-CREST from Japan Agency for Medical
25 Research and development, AMED (16gm0810005h0102). The authors acknowledge Dr. K.
26 Nagayama for their help and discussion during experiments.

27

28

29 **Abstract**

30 Although elucidation of the mechanism of aortic aneurysm rupture is important, the
31 characteristics of crack initiation and propagation sites remain unknown. To determine the
32 microscopic properties of these sites, the characteristics of local **strains** and constituents at
33 crack initiation and propagation sites were investigated during biaxial stretching of porcine
34 thoracic aortas (PTAs). PTAs were sliced into approximately 50- μm -thick sections, and the
35 center of the sections was made especially thin using our previously developed technique.
36 Alpha-elastin and cell nuclei were fluorescently labeled as indices of local elastin density
37 and as a strain marker, respectively. Birefringence and second harmonic generation (SHG)
38 light images were used to determine local collagen distributions. The specimens were then
39 stretched biaxially with a laboratory-made tensile tester under a fluorescent microscope
40 equipped with a birefringence imaging system. Local strains were calculated from the local
41 displacement of the cell nuclei. The degree of alignment and density of local collagen fibers
42 were measured from retardance and SHG images. The strain distributions, specifically the
43 first and second principal, and maximum shear strains, fluorescent intensity of α -elastin, and
44 degree of alignment of collagen fibers, showed insignificant differences between the crack
45 initiation sites and other sites. The retardance and intensity of SHG light at the crack
46 initiation sites were significantly lower than those at other sites for all ($n = 6$) specimens.
47 **Cracks tended to propagate** along the local direction of the collagen fibers. These results
48 indicate that the local density and direction of collagen fibers play an important role in aorta
49 rupture.

50

51 **Key Words:** Thoracic Aorta, Biaxial Stretch Rupture, Local Composition, Second
52 Harmonic Imaging Microscopy, Birefringence Imaging Microscopy

53

54 **1. Introduction**

55 Large aneurysms tend to be at a high risk of rupture due to high wall stress according to
56 Laplace's law. In clinical practices, a critical diameter of approximately 5.5 cm is used as
57 the criterion for surgical repair for patients with thoracic aortic aneurysms (TAAs). However,
58 TAAs smaller than this size can also rupture (Cambria et al. 1995; Coady et al. 1997).
59 Although the thickness of aneurysms should be negatively correlated with the rupture risk
60 because thin walls lead to high local wall stress (Raghavan et al. 2006), no significant
61 difference in thickness has been reported between ruptured and unruptured aneurysmal
62 specimens (Raghavan et al. 2011). With the progression of the disease, the strength of
63 aneurysmal tissue may continue to decrease, and the vessel may finally succumb to the
64 physiological wall stress, resulting in rupture (Raghavan et al. 1996). The tensile strength of
65 TAAs was reported to be significantly lower than that of normal vessels (He and Roach
66 1994). However, there have also been studies that found no significant differences between
67 healthy and aneurysmal specimens (Garcia-Herrera et al. 2012; Iliopoulos et al. 2009;
68 Raghavan et al. 2011; Sokolis et al. 2012). Thus, the factors that influence aneurysm rupture
69 remain unknown.

70 Aortic tissue is a composite material mainly consisting of cells, collagen, and elastin.
71 Those constituents are important factors that affect the strength of the aortas. In aneurysms,
72 a decrease in the elastin is commonly reported (He and Roach 1994; Iliopoulos et al. 2009),
73 and this might cause an increase in wall stiffness (He and Roach 1994). The volume fraction
74 of collagen and ground substance was reported to be higher in aneurysms in one study (He
75 and Roach 1994), and collagen content in aneurysmal specimens was not significantly
76 different from that in normal tissue in another study (Iliopoulos et al. 2009). Since the
77 tensile strength of collagen is the highest among the constituents of the aortas (Fung 1981),
78 increased or unchanged collagen content in aneurysmal walls seems paradoxical.

79 One possible explanation for this paradox is that these studies averaged the parameters in
80 tissues and did not focus on local values in the aortas. Rupture can occur from even a small
81 region with weakened strength in the aortas. We previously developed a pressure-imposed
82 test (bulge test) system (Ohashi et al. 2003) and found that strain distribution in TAA

83 specimens was more heterogeneous than that in healthy porcine thoracic aortas (PTAs)
84 (Sugita et al. 2011). Moreover, all PTA specimens eventually ruptured, whereas some TAA
85 specimens ruptured at much lower stress than average and other TAA specimens did not
86 rupture even under more than 4000 mmHg of pressure (Sugita et al. 2011). These results
87 indicate that locally weak regions in aneurysmal walls are points of failure. Thus, it is
88 important to investigate the relationship between the local properties of the aorta and the
89 rupture site. Although the effects of the histological and mechanical properties on a ruptured
90 site were previously investigated at the millimeter scale (Raghavan et al. 2011), more
91 microscopic analyses should be performed to evaluate tissue heterogeneity.

92 To determine the microscopic properties at the crack initiation site, *the bulge test is not*
93 *suitable for it is difficult to keep specimen focused under a microscope, and thus* we
94 developed a biaxial stretch tester placed on an inverted microscope (Sugita and Matsumoto
95 2013b). Using this device, aortic tissues were successfully stretched biaxially until failure *in*
96 *a single focal plane*, and their crack initiation points were successfully observed under a
97 microscope (Sugita and Matsumoto 2013b). In the present study, we measured the
98 distributions of elastin and collagen and the strain distributions in the biaxially stretched
99 healthy PTA specimens to investigate the factors that affect crack initiation.

100

101 **2. Materials and methods**

102 **2.1. Specimen preparation**

103 Healthy PTA specimens were used. To induce rupture at the center of the aortic
104 specimen under biaxial stretch, aortic slices thinned at the center were prepared according to
105 the procedure described in our previous study (Sugita and Matsumoto 2013b). Briefly, a
106 PTA block with dimensions of 15 mm in the longitudinal direction and 20 mm in the
107 circumferential direction was sandwiched between two metal plates with a hole at the center
108 and compressed by 40% in the radial direction. During this process, the center of the
109 specimen was less compressed than the periphery because of the holes in the metal plates.
110 The block was frozen at -80°C for 10 min to fix the shape of the specimen, embedded in
111 Tissue Mount (Chiba Medical, Saitama, Japan), and sectioned with a cryotome (CM3050SIV,

112 Leica Microsystems, Wetzlar, Germany) into 50- μ m slices perpendicular to its radial
113 direction. The specimens were kept at -80°C until tested and only specimens obtained from
114 the middle of one-third of the aorta in the radial direction were used. When the specimens
115 were thawed, the compression in the specimen periphery loosened more than the
116 compression in the center, causing the center of the specimen to appear thinner.

117

118 **2.2. Staining**

119 The specimens were immersed in 2% bovine serum albumin (BSA) for 1 h for blocking.
120 For elastin staining, specimens were incubated with the antimouse antibody of elastin
121 (Sc-58756, Santa Cruz Biotechnology, Santa Cruz, CA, USA) diluted 1/50 in PBS(-)
122 including 0.2% BSA for 1.5 h, followed by incubation with secondary antibody (anti IgG
123 Alexa fluor 488, A11059, Invitrogen, Carlsbad, CA, USA) diluted 1/50 in PBS(-) including
124 0.2% BSA for 1 h. To measure strain distribution in the specimens, the specimens were
125 incubated with 10 $\mu\text{g}/\text{ml}$ Hoechst 33342 solution (Invitrogen) for 30 min to visualize the
126 cell nuclei. All processes were performed at room temperature.

127

128 **2.3. Equi-biaxial tensile test**

129 Specimens were stretched equi-biaxially in both the circumferential and longitudinal
130 directions using a laboratory-made equi-biaxial stretching device (Sugita and Matsumoto
131 2013b). Briefly, a specimen was glued onto [polyethylene terephthalate \(PET\) film sheet and](#)
132 [part of PET film with a hole at the center and the sheet was glued onto](#) a metal frame with a
133 hole. The metal frame was then moved stepwise by 0.5 mm at each step toward a metal
134 hollow cylinder to stretch the specimen biaxially. This setup was placed under a fluorescent
135 microscope (IX71, Olympus, Tokyo, Japan). At each step, phase contrast, fluorescent, and
136 retardance images of the specimen were captured on a charge-coupled device camera
137 equipped with a birefringence imaging system Pol-Scope (Abrio-LS, CRi, Woburn, MA,
138 USA) (Oldenbourg 1996) through a 2 \times objective lens (PLAPON 2 \times , Olympus). This system
139 enabled us to analyze the retardance as an index of collagen density and slow axis azimuth
140 as the collagen fiber angle of the samples at each pixel on the charge-coupled device. [When](#)

141 light passes through a birefringent material, the light wave is separated into two
142 orthogonally polarized waves that travel at different speed, causing a phase shift or
143 retardance and retardance correlated significantly with collagen volume as confirmed in our
144 previous study (Sugita and Matsumoto 2013c). Images were repeatedly captured, and the
145 metal frame was moved continuously until specimen failure. High-speed (300 frames/s)
146 images were recorded simultaneously with a digital camera (Exilim EX-F1, Casio
147 Computer, Tokyo, Japan) to determine the crack initiation site. Analysis was performed six
148 out of ten specimens because cracks initiated from edge of thin sample region in other four
149 specimens perhaps because of the stress concentration in these area (Sugita and Matsumoto
150 2013b).

151

152 **2.4. Second harmonic generation light observation**

153 Specimen glued onto a PET film was set under the a two-photon-excited microscope
154 (FV1200MPE, Olympus), and the second harmonic generation (SHG) light image of the
155 specimen was captured as previously reported (Sugita and Matsumoto 2017). Briefly, the
156 power of a mode-locked Ti:sapphire laser (wavelength = 800 nm, pulse width = 100 fs,
157 repetition rate = 80 MHz, laser power = 3 mW) was reduced to 4.5%, and the laser was
158 focused on specimens through an 10× objective lens (UMPLan FLN 10XW, NA = 0.30,
159 Olympus). The generated SHG signal was collected in the backward direction through a
160 dichroic mirror (485 nm) and a band pass filter (400 ± 5 nm). Before and after the biaxial
161 stretch test, 4×4 images in both the longitudinal and circumferential directions were
162 captured across the wall with a Z-interval of 10 μ m.

163 These stack images were converted into projection images of 2D sum slices in the
164 circumferential-longitudinal plane using image analysis software (ImageJ 1.47v, National
165 Institutes of Health, Bethesda, MD, USA). The 4×4 images in the longitudinal and
166 circumferential directions were then merged using a “photomerge” function in image
167 analysis software (Photoshop CS6, Adobe Systems, San Jose, CA, USA).

168 Total of eleven unstained specimens were used in this experiment. Six specimens were
169 analyzed and five specimens were excluded because crack initiated in the edge of thin

170 sample region. After imaging, the biaxial test was performed on the specimens as described
 171 in the Section 2.3. The specimens were then peeled off from the metal plate carefully not to
 172 distort them and their SHG images after crack propagation were captured.

173

174 **2.5. Strain analysis**

175 Strain distribution was obtained from images of fluorescently labeled cell nuclei during
 176 biaxial stretching as we previously reported (Sugita and Matsumoto 2013a). Briefly, local
 177 displacement was measured every 10 pixels (approximately 50 μm) with **digital image**
 178 **correlation software** (Flow-vec v. 4.9, Library, Tokyo, Japan). In a pair of sequential images,
 179 an analysis region of 31×31 pixels (approximately $150 \times 150 \mu\text{m}^2$) was selected in the first
 180 image, and a region with the same size and the highest correlation with the interrogation
 181 region was searched in the second image with a search size of 101×101 pixels
 182 (approximately $500 \times 500 \mu\text{m}^2$). From the displacement data, the components of the 2D
 183 strain tensor in the circumferential and longitudinal directions (ε_{CC} , ε_{LL} , $\varepsilon_{CL} + \varepsilon_{LC}$) were
 184 locally calculated as follows:

$$185 \quad \varepsilon_{CC} = \frac{X_{(I+1,J)'} - X_{(I,J)'}}{X_{(I+1,J)} - X_{(I,J)}} \quad (1)$$

$$186 \quad \varepsilon_{LL} = \frac{Y_{(I,J+1)'} - Y_{(I,J)'}}{Y_{(I,J+1)} - Y_{(I,J)}} \quad (2)$$

$$187 \quad \varepsilon_{CL} + \varepsilon_{LC} = \frac{X_{(I,J+1)'} - X_{(I,J)'}}{Y_{(I,J+1)} - Y_{(I,J)}} + \frac{Y_{(I+1,J)'} - Y_{(I,J)'}}{X_{(I+1,J)} - X_{(I,J)}}, \quad (3),$$

188 where $\langle I, J \rangle$ represents the I th and J th center points of the analysis window in the
 189 circumferential and longitudinal directions, respectively; X and Y are coordinates in the
 190 circumferential and longitudinal directions; and the apostrophe (') indicates the coordinates
 191 after displacement. These strains were calculated at each displacement step, and the
 192 cumulative strains from the zero load state were calculated. Finally, the first ε_1 and second
 193 ε_2 principal strains, the maximum shear strain γ_{\max} , and the areal strains $\varepsilon_{\text{area}}$ were calculated
 194 from the following equations:

$$\varepsilon_1 = \frac{\varepsilon_{CC} + \varepsilon_{LL}}{2} + \sqrt{\frac{(\varepsilon_{CC} - \varepsilon_{LL})^2}{2} + \left(\frac{\varepsilon_{CL} + \varepsilon_{LC}}{4}\right)^2} \quad (4)$$

$$\varepsilon_2 = \frac{\varepsilon_{CC} + \varepsilon_{LL}}{2} - \sqrt{\frac{(\varepsilon_{CC} - \varepsilon_{LL})^2}{2} + \left(\frac{\varepsilon_{CL} + \varepsilon_{LC}}{4}\right)^2} \quad (5)$$

$$\gamma = \sqrt{(\varepsilon_{CC} - \varepsilon_{LL})^2 - (\varepsilon_{CL})^2} \quad (6)$$

$$\varepsilon_{Area} = (1 + \varepsilon_{CC})(1 + \varepsilon_{LL}) - \varepsilon_{CL}\varepsilon_{LC} \quad (7)$$

Strain analysis was first performed in all areas of the specimen inside the metal cylinder (6 mm in diameter), and only data obtained from thin center region (~2 mm in diameter at no load state) were used for the analysis to exclude boundary effects.

2.6. Elastin and collagen density analysis

Fluorescent intensities in the elastin image were also averaged for each $50 \times 50 \mu\text{m}^2$ area, which were the same areas used in the strain analysis, as indices of local elastin density. To investigate the effect of the distribution of collagen fibers on the fracture, retardance was averaged for each $50 \times 50 \mu\text{m}^2$ area. Since retardance is affected by a combination of density and the alignment agreement of collagen fibers (see Online Resource S1), SHG images were also analyzed. We confirmed that intensity can be used as an index of the density of collagen fibers because the SHG intensity linearly correlated with the density of the collagen fibers, and the degree of alignment for the collagen fibers did not affect the intensity of the SHG image (see Online Resource S2).

2.7. Determination of crack initiation and propagation sites

The crack initiation point was determined using high-speed camera images. The crack initiation site was identified as a local 10×10 pixel ($50 \times 50 \mu\text{m}^2$) area including the crack initiation point and the surrounding 5×5 area ($250 \times 250 \mu\text{m}^2$). Other areas were termed “other sites.”

Crack positions in SHG images captured before the biaxial tensile test were determined from cracks and collagen fiber patterns in SHG images captured after rupture. For analysis of the alignment and orientation of collagen fibers, $250 \times 250 \mu\text{m}^2$ areas along the crack in

222 the SHG image were selected as the crack propagation sites. Areas in which the crack
 223 propagated in a zigzag fashion were excluded.

224

225 **2.8. Alignment and orientation of collagen fibers**

226 As described in a previous study (Sugita and Matsumoto 2017), the alignment
 227 consistency of collagen fibers was analyzed for the crack initiation and propagation sites
 228 determined in Section 2.7. Briefly, local images at the crack initiation and propagation sites
 229 were processed using two-dimensional fast Fourier transform to obtain power spectrum
 230 images (PSIs) of the fibers. Since high intensities were observed in directions perpendicular
 231 to the fiber directions for the obtained PSI (Petroll et al. 1993), average intensity was
 232 calculated for every 10° area around the origin in the PSI and was normalized by the
 233 summation of the average intensity at each angle to give the probability distribution of
 234 collagen fiber orientations. The probability distribution was then fitted with a Gaussian
 235 function:

$$236 \quad P = P_{base} + (P_{peak} - P_{base}) \exp\left\{-\frac{(\alpha - \alpha_{average})^2}{2\sigma^2}\right\}, \quad (8)$$

237 where P is the probability of the fiber angle α , and P_{base} , P_{peak} , $\alpha_{average}$, and σ are fitting
 238 constants that indicate the base level, maximum value, average angle, and standard
 239 deviation (SD) of the Gaussian distribution, respectively. Since the parameter σ should be
 240 high when the alignment consistency of the collagen fibers in the original image is low, σ
 241 was used to evaluate the alignment inconsistency of the collagen fibers. When the
 242 probability $P(\alpha)$ at angle α was 1.5 times higher than the average of P , α was determined to
 243 be the direction in which the collagen fibers were aligned with high probability. The number
 244 of directions was 3.7 ± 1.0 (mean \pm SD) in 18 directions of α .

245

246 **2.9. Crack direction**

247 Crack directions were analyzed both microscopically using SHG images captured under
 248 the microscope and macroscopically using images captured with a digital camera.

249 In the microscopic analysis, the crack directions at the crack initiation and propagation

250 sites determined in Section 2.7 were measured. A 100- μm -long line segment was fitted to
251 the shape of each crack visually at the crack initiation and propagation sites in the SHG
252 images captured after rupture, and their angles were measured using ImageJ.

253 In the macroscopic analysis, after whole sample images were captured with a digital
254 camera (CX3, Ricoh Imaging, Tokyo, Japan), the crack direction at the crack initiation
255 position was measured by fitting a 300- μm -long line segment. Similarly, the direction of
256 each crack was determined by fitting a 300- μm -long line segment at both ends of the crack,
257 and these directions were compared with the directions of the cracks at the crack initiation
258 sites identified using microscopic analysis.

259

260 **2.10. Statistics**

261 For each specimen, mean \pm SD was calculated both at the crack initiation sites and at
262 other sites, and the results were compared using Student's unpaired *t*-test [within each](#)
263 [specimen](#). The average values at both sites in each specimen were then calculated for all six
264 specimens and compared using [Wilcoxon signed-ranks test as non-parametric and paired](#)
265 [test](#). [Since the number of the crack end sites were double of the number of the crack](#)
266 [initiation sites, comparison of the difference in the crack direction was performed using the](#)
267 [Mann-Whitney U-test](#). The significance level was set at 0.05.

268

269 **3. Results**

270 **3.1. Local strains**

271 Figure 1 shows the characteristics of local strains at the crack initiation sites. All strain
272 distributions such as the first principal strain (Fig. 1a), the second principal strain (Fig. 1b),
273 the maximum shear strain (Fig. 1c), and the areal strain (Fig. 1d) during biaxial stretching
274 were heterogeneous as reported in a previous study (Sugita and Matsumoto 2013a). For
275 comparison of strains between the crack initiation sites and the other sites in all six
276 specimens (Fig. 1e–h), only areal strain at the crack initiation sites was significantly higher
277 than that at the other sites (Fig. 1h). However, when strains were compared in each
278 specimen, significantly higher strains were not always observed at the crack initiation sites

279 compared with the other sites (3 of 6 specimens for the first principal strain [Fig. 1e], 0 of 6
280 specimens for the second principal strain [Fig. 1f], 1 of 6 specimen for the shear strain [Fig.
281 1g], and 2 of 6 specimens for the areal strain [Fig. 1h]). These results indicate that the crack
282 initiation sites were not determined by high local strain at this scale (~50 μm).

283

284 **3.2. Local elastin distribution**

285 Figure 2a shows a typical image of fluorescently labeled elastin. The intensity of
286 fluorescently labeled elastin was heterogeneous and significantly higher at the crack
287 initiation sites (white box area in Fig. 2a) for 2 of 6 specimens and lower for 2 of 6
288 specimens (Fig. 2b). These results indicate that the crack initiation sites were not
289 determined by elastin distribution either.

290 **3.3. Retardance distribution**

291 Figure 3 shows the characteristics of birefringence distribution just before rupture. In the
292 retardance image, which shows an index of collagen density distribution (Fig. 3a),
293 retardance was low at the crack initiation sites. Statistical analysis showed that retardance at
294 the crack initiation sites was significantly lower than that at other sites for both the average
295 value of all the specimens and comparison within a single specimen (6 of 6 specimens) (Fig.
296 3c).

297 A typical image of azimuth distribution in a specimen is shown in Fig. 3b. Collagen
298 fibers aligned in the circumferential direction and the azimuth changed slightly in several
299 local areas. The slow axis azimuth at the crack initiation sites was significantly higher in 2
300 of 6 specimens than that at the other sites but was lower in 2 of 6 specimens (Fig. 3d).

301 We had expected that the retardance might change at failure because collagen fibers
302 might be broken locally at the crack initiation sites. However, changes in the retardance
303 between the period just before rupture and the previous loading step at the crack initiation
304 sites showed no clear trend: the changes in the retardance was significantly higher in some
305 specimens (3 of 6 specimens) but lower in others (2 of 6 specimens; Fig. S3). Since
306 collagen density during a stretch should not change at each site, changes in retardance may
307 indicate changes in the alignment consistency of collagen fibers. Thus, these results indicate

308 that changes in the alignment consistency of collagen fibers do not correlate with the crack
309 initiation.

310

311 **3.4. SHG light distribution at crack initiation site**

312 The retardance is affected by both the collagen density and alignment consistency of
313 collagen fibers. We thus analyzed the SHG signal, which is generated from collagen fibers
314 in the aorta. Figure 4 shows a typical image of SHG light in the specimen before (Fig. 4a)
315 and after (Fig. 4b) the biaxial test. The average intensity at the crack initiation sites for all
316 specimens was significantly lower than that at the other sites (Fig. 4c). This significant
317 difference was also found in each specimen (6 of 6 specimens).

318 Fitting parameter σ , which shows the alignment inconsistency of collagen fibers, shows
319 insignificant differences between the crack initiation sites and the other sites (Fig. 4d). This
320 indicates that low retardance at the crack initiation sites is due to low collagen density rather
321 than high alignment inconsistency in the collagen fibers.

322 These results indicate that cracks propagate from low collagen density sites.

323

324 **3.5. Crack propagation in the aorta**

325 An SHG image obtained after rupture (Fig. 4b) showed that the cracks observed under
326 the microscope propagated in zigzags, and the cracks partially ran along the longitudinal
327 direction in the macroscopic view. In 64% (25 of 39) of the crack propagation sites, crack
328 directions corresponded to the directions of the collagen fibers with high probability for
329 collagen fibers aligned in the circumferential direction (Fig. 5a) or approximately 45° from
330 the circumferential and longitudinal (Fig. 5b) directions, indicating that the cracks **tended to**
331 **propagate along the directions of the collagen fibers.** **However,** some cracks ran in other
332 directions (Fig. 5c), **indicating that other factors may be involved in crack direction.** Crack
333 angle distribution at crack propagation areas is shown in Fig. 5d. The local angle of the
334 crack direction, which was determined using a 100- μm -long line segment fitted locally to
335 the crack in the microscopic image, seems to run in several preferred direction such as $\pm 30^\circ$
336 and $\pm 0^\circ$ from the circumferential direction.

337 Macroscopically, the cracks seem to run in the circumferential direction rather than in the
338 longitudinal direction (Fig. S4). Figure 5e shows the absolute value of the local crack angle
339 from the circumferential direction, which was determined to be the 300- μm -long line
340 segment in images captured with a digital camera. The angle at crack initiation sites ($41^\circ \pm$
341 20°) tended to be higher than that at the ends of the crack sites ($20^\circ \pm 19^\circ$) though it was
342 insignificant ($p = 0.06$), indicating that the cracks run in the relatively longitudinal direction
343 at the crack initiation sites, then propagate in the relatively circumferential direction on the
344 macro scale.

345

346 4. Discussion

347 In this study, the effects of local mechanical and morphological properties on crack
348 initiation and propagation were investigated using healthy PTA specimens. We found that
349 crack initiation and propagation depended on the local structure of collagen fibers; cracks
350 were initiated at regions with a low density of collagen fibers and propagated along the
351 direction of the fibers. These results are reasonable because the elastic modulus and tensile
352 strength of collagen fibers are higher than those of other constituents in the aortas (Fung
353 1981), and collagen fibers are considered principal load-bearing elements in high strain and
354 stress regions. In addition to that, recent studies have stated mechanics of arterial wall
355 focusing on collagen fiber distributions which affects material characterization of artery
356 (Gasser et al. 2006) and ascending thoracic aortic aneurysms (Sassani et al. 2015). However,
357 this is the first study, to our knowledge, to confirm that the local density of collagen fibers
358 plays an important role in the wall strength of biaxially stretched aortas on the microscopic
359 scale. Strain distribution in TAA specimens was more heterogeneous than that in healthy
360 PTAs (Sugita et al. 2011), and decreased elastin has been reported in aneurysms (He and
361 Roach 1994; Iliopoulos et al. 2009). Such heterogeneity and changes in constituents may
362 produce local weak points with a low density of collagen fibers in aneurysmal tissues. Stress
363 concentration occurs at these points, and the crack may initiate from these points. This
364 might be the reason for the rupture of smaller aneurysms (Cambria et al. 1995; Coady et al.
365 1997).

366 Although the retardance and intensity in SHG images were significantly lower at the
367 crack initiation sites than at other sites in this study, the values at these sites were not always
368 the lowest. Furthermore, holes were sometimes observed in specimens, and cracks were
369 initiated in other regions. Although we had anticipated that cracks would initiate from sites
370 with the lowest retardance, **not all** cracks initiated from **that** regions. These results indicate
371 that other factors must be involved in rupture, and such factors should be elucidated to
372 precisely determine the rupture risk. Since the aortic media comprise both types I and III
373 collagen and a decrease in type I and an increase in type III collagen correlate significantly
374 with a decrease in the elastic modulus of tendons (Wan et al. 2014), the density
375 heterogeneity of collagen subtypes may affect the local strength of the aorta. The
376 connecting force between fibers is another possible candidate that may affect the local
377 strength.

378 One might think that other possible reason influencing on the position of the crack
379 initiation sites can be a local thickness. The local thickness of the specimen was evaluated
380 from intensity of a bright field image of the specimen after confirming in a preliminary
381 study that the intensity correlated significantly with local thickness of specimen measured
382 directly with a laser microscope. The cracks initiated from the thinner area in only 2 out of 6
383 specimens, indicating that local thickness was not a determinant factor of the crack
384 initiation sites in this study.

385 Basically, cracks run in the same direction as collagen fibers. In the thoracic aortas, two
386 distinct collagen fiber families were observed, and their azimuthal mean angles in the
387 circumferential-axial plane were reported to be -27.19° and 27.75° from the circumferential
388 direction (Schriebl et al. 2011). This may be the reason why the probability of a large local
389 crack angle was high at approximately $\pm 30^\circ$ from the circumferential direction in this study
390 (Fig. 5d). After crack initiation, most cracks propagated and changed direction to the
391 circumferential direction (Fig. 5e), resulting in crack shapes that were aligned in the
392 circumferential direction (Fig. S4a). This result was in good agreement with a previous
393 study in which all cracks ran in the circumferential direction in pressure-imposed tests for
394 PTA specimens (Sugita et al. 2011).

395 We previously reported that the first principal strain was inversely correlated with
396 retardance (Sugita and Matsumoto 2013a). This is likely because cracks run from high
397 strain regions because the cracks were initiated at low retardance regions in this study.
398 However, this study showed that the first principal strain was not always higher at the crack
399 initiation sites than at the other sites (Fig. 1e) although areal strains tended to be high (Fig.
400 1h). Since the correlation coefficient was relatively low (-0.077) in a previous study (Sugita
401 and Matsumoto 2013a), collagen distribution may play a more important role than strains in
402 vessel wall strength. *In bulge test of ascending aortic thoracic aneurysms, rupture occurred
403 at one of strain concentration area (Davis et al. 2016). Since thickness of the specimen in
404 the Davis et al. might not be uniform, thin specimen area tends to become high strain area,
405 which may result in rupture. In this study, since specimen with relatively uniform thickness
406 was prepared by cutting specimen, collagen distribution might play a more dominant role
407 than the strain on the wall strength. Heterogeneous distribution in mechanical properties of
408 collagen fibers might cause crack initiation in the area where strain was not so high.*

409 To evaluate the size of the crack initiation sites, analysis using other sizes for crack
410 initiation sites was also performed. When the size of the crack initiation site was changed
411 from $250 \times 250 \mu\text{m}^2$ to 350×350 and $150 \times 150 \mu\text{m}^2$, retardance at the crack initiation sites
412 was still significantly lower than that at other sites (Fig. S5a and b). Thus, the size of the
413 crack initiation sites did not have much impact on the result in this study.

414 There were some limitations in this study. First, tissues were frozen to shape the
415 specimens. This may have caused changes in the mechanical properties of the specimens.
416 However, as discussed in our previous paper (Sugita and Matsumoto 2013b), freezing has
417 been reported to affect the mechanical behavior of a small strain region either significantly
418 (Venkatasubramanian et al. 2006) or insignificantly (Masson et al. 2009; Stemper et al.
419 2007), and the effect of freezing on the collagen fibers appears to be low (Goh et al. 2010).
420 Thus, we believe that the influence of freezing on the results of this study was negligible.
421 Second, specimens were equi-biaxially stretched because we plan to apply this analysis
422 method to aneurysmal tissue, which is thought to be stretched biaxially in vivo, in a future
423 study. However, healthy PTA, which is not biaxially stretched in vivo, was used in this

424 study because the aortas have a hollow cylindrical shape. Third, for modification of the
425 shape of the specimens, which enabled us to observe the crack initiation sites during biaxial
426 stretching and to observe SHG light from the specimens, the specimens were sliced into
427 50- μm sections, which may have affected the collagen structure around the surface area.
428 However, thick specimens, which were sliced into 150- μm sections, showed a similar result
429 in that retardance was significantly lower at the crack initiation sites than at the other sites
430 (Fig. S6), indicating that the effect of slicing the specimen would have been very small.

431

432 **5. Conclusions**

433 Constituent and mechanical characteristics of crack initiation sites were studied in
434 healthy PTAs subjected to equi-biaxial stretching. Although there were insignificant
435 differences between the sites with regard to local strains and elastin distribution, the
436 retardance and intensity of SHG images were significantly lower at the crack initiation sites,
437 indicating that low local collagen density increases the risk of rupture. Furthermore, cracks
438 tended to propagate along the direction of the collagen fibers. These results indicate that the
439 local density and direction of collagen fibers play an important role in aorta rupture.

440

441 **Conflicts of interest statement**

442 There are no conflicts of interest.

443

444 **References**

- 445 Cambria RA, Gloviczki P, Stanson AW, Cherry KJ, Jr., Bower TC, Hallett JW, Jr., Pairolero
446 PC (1995) Outcome and expansion rate of 57 thoracoabdominal aortic aneurysms
447 managed nonoperatively *Am J Surg* 170:213-217
448 doi:10.1016/S0002-9610(99)80289-X
- 449 Coady MA, Rizzo JA, Hammond GL, Mandapati D, Darr U, Kopf GS, Elefteriades JA
450 (1997) What is the appropriate size criterion for resection of thoracic aortic
451 aneurysms? *J Thorac Cardiovasc Surg* 113:476-491
452 doi:10.1016/S0022-5223(97)70360-X
- 453 [Davis FM, Luo Y, Avril S, Duprey A, Lu J \(2016\) Local mechanical properties of human
454 ascending thoracic aneurysms *J Mech Behav Biomed Mater* 61:235-249
455 doi:10.1016/j.jmbbm.2016.03.025](#)
- 456 Fung YC (1981) Biomechanics: mechanical properties of living tissues. Biomechanics:
457 mechanical properties of living tissues, 2nd edn. Springer-Verlag, New York
- 458 Garcia-Herrera CM, Atienza JM, Rojo FJ, Claes E, Guinea GV, Celentano DJ,
459 Garcia-Montero C, Burgos RL (2012) Mechanical behaviour and rupture of normal
460 and pathological human ascending aortic wall *Med Biol Eng Comput* 50:559-566
461 doi:10.1007/s11517-012-0876-x
- 462 [Gasser TC, Ogden RW, Holzapfel GA \(2006\) Hyperelastic modelling of arterial layers with
463 distributed collagen fibre orientations *J R Soc Interface* 3:15-35
464 doi:10.1098/rsif.2005.0073](#)
- 465 Goh KL, Chen Y, Chou SM, Listrat A, Bechet D, Wess TJ (2010) Effects of frozen storage
466 temperature on the elasticity of tendons from a small murine model animal
467 4:1613-1617 doi:10.1017/S1751731110000698
- 468 He CM, Roach MR (1994) The composition and mechanical properties of abdominal aortic
469 aneurysms *J Vasc Surg* 20:6-13 doi:10.1016/0741-5214(94)90169-4
- 470 Iliopoulos DC, Kritharis EP, Giagini AT, Papadodima SA, Sokolis DP (2009) Ascending
471 thoracic aortic aneurysms are associated with compositional remodeling and vessel
472 stiffening but not weakening in age-matched subjects *J Thorac Cardiovasc Surg*

- 473 137:101-109 doi:10.1016/j.jtcvs.2008.07.023
- 474 Masson I, Fialaire-Legendre A, Godin C, Boutouyrie P, Bierling P, Zidi M (2009)
- 475 Mechanical properties of arteries cryopreserved at -80 degrees C and -150 degrees C
- 476 Med Eng Phys 31:825-832 doi:10.1016/j.medengphy.2009.03.009
- 477 Ohashi T, Sugita S, Matsumoto T, Kumagai K, Akimoto H, Tabayashi K, Sato M (2003)
- 478 Rupture properties of blood vessel walls measured by pressure-imposed test JSME
- 479 Int J Ser C 46:1290-1296 doi:10.1299/jsmec.46.1290
- 480 Oldenbourg R (1996) A new view on polarization microscopy Nature 381:811-812
- 481 doi:10.1038/381811a0
- 482 Petroll WM, Cavanagh HD, Barry P, Andrews P, Jester JV (1993) Quantitative analysis of
- 483 stress fiber orientation during corneal wound contraction J Cell Sci 104:353-363
- 484 Raghavan ML, Hanaoka MM, Kratzberg JA, de Lourdes Higuchi M, da Silva ES (2011)
- 485 Biomechanical failure properties and microstructural content of ruptured and
- 486 unruptured abdominal aortic aneurysms J Biomech 44:2501-2507
- 487 doi:10.1016/j.jbiomech.2011.06.004
- 488 Raghavan ML, Kratzberg J, Castro de Tolosa EM, Hanaoka MM, Walker P, da Silva ES
- 489 (2006) Regional distribution of wall thickness and failure properties of human
- 490 abdominal aortic aneurysm J Biomech 39:3010-3016
- 491 doi:10.1016/j.jbiomech.2005.10.021
- 492 Raghavan ML, Webster MW, Vorp DA (1996) Ex vivo biomechanical behavior of
- 493 abdominal aortic aneurysm: assessment using a new mathematical model Ann
- 494 Biomed Eng 24:573-582
- 495 [Sassani SG, Tsangaris S, Sokolis DP \(2015\) Layer- and region-specific material](#)
- 496 [characterization of ascending thoracic aortic aneurysms by microstructure-based](#)
- 497 [models J Biomech 48:3757-3765 doi:10.1016/j.jbiomech.2015.08.028](#)
- 498 Schriefl AJ, Zeindlinger G, Pierce DM, Regitnig P, Holzapfel GA (2011) Determination of
- 499 the layer-specific distributed collagen fibre orientations in human thoracic and
- 500 abdominal aortas and common iliac arteries J R Soc Interface 9:1275-1286
- 501 doi:10.1098/rsif.2011.0727

- 502 Sokolis DP, Kritharis EP, Giagini AT, Lampropoulos KM, Papadodima SA, Iliopoulos DC
503 (2012) Biomechanical response of ascending thoracic aortic aneurysms: association
504 with structural remodelling *Comput Methods Biomech Biomed Engin* 15:231-248
505 doi:10.1080/10255842.2010.522186
- 506 Stemper BD, Yoganandan N, Stineman MR, Gennarelli TA, Baisden JL, Pintar FA (2007)
507 Mechanics of fresh, refrigerated, and frozen arterial tissue *J Surg Res* 139:236-242
508 doi:10.1016/j.jss.2006.09.001
- 509 Sugita S, Matsumoto T (2013a) Heterogeneity of deformation of aortic wall at the
510 microscopic level: Contribution of heterogeneous distribution of collagen fibers in
511 the wall *Bio-Med Mater Eng* 23:447-461 doi:10.3233/BME-130771
- 512 Sugita S, Matsumoto T (2013b) Novel biaxial tensile test for studying aortic failure
513 phenomena at a microscopic level *Biomed Eng OnLine* 12:3
514 doi:10.1186/1475-925x-12-3
- 515 [Sugita S, Matsumoto T \(2013c\) Quantitative measurement of the distribution and alignment
516 of collagen fibers in unfixed aortic tissues *J Biomech* 46:1403-1407
517 doi:10.1016/j.jbiomech.2013.02.003](#)
- 518 Sugita S, Matsumoto T (2017) Multiphoton microscopy observations of 3D elastin and
519 collagen fiber microstructure changes during pressurization in aortic media *Biomech
520 Model Mechanobiol* 16:763-773 doi:10.1007/s10237-016-0851-9
- 521 Sugita S, Matsumoto T, Ohashi T, Kumagai K, Akimoto H, Tabayashi K, Sato M (2011)
522 Evaluation of rupture properties of thoracic aortic aneurysms in a pressure-imposed
523 test for rupture risk estimation *Cardiovasc Eng Technol* 3:41-51
524 doi:10.1007/s13239-011-0067-1
- 525 Venkatasubramanian RT, Grassl ED, Barocas VH, Lafontaine D, Bischof JC (2006) Effects
526 of freezing and cryopreservation on the mechanical properties of arteries *Ann
527 Biomed Eng* 34:823-832 doi:10.1007/s10439-005-9044-x
- 528 Wan C, Hao Z, Wen S, Leng H (2014) A quantitative study of the relationship between the
529 distribution of different types of collagen and the mechanical behavior of rabbit
530 medial collateral ligaments *PLoS ONE* 9:e103363

531 [doi:10.1371/journal.pone.0103363](https://doi.org/10.1371/journal.pone.0103363)

532

533 **Figures Captions**

534

535 **Fig. 1** Characteristics of local strains at crack initiation sites just before rupture. (a–d)
536 Typical distributions of (a) the first principal, (b) the second principal, (c) the maximum
537 shear, (d) and areal strains in specimen #1. Red boxes in images show the crack initiation
538 sites. Bar in (d) = 1 mm applies to all images. (e–h) Comparison of (e) the first principal, (f)
539 the second principal, (g) the maximum shear, (h) and areal strains between the crack
540 initiation site and other sites for each specimen. Linear and broken lines show data for $p <$
541 0.05 and NS, respectively, for comparison between the crack initiation site and other sites
542 within a single specimen. Each mark represents the average within a single specimen

543

544 **Fig. 2** Characteristics of local amount of elastin at crack initiation sites just before rupture.
545 (a) Typical fluorescent image of elastin in specimen #2. A white box shows the crack
546 initiation sites. Bar = 1 mm. (b) Comparison of mean intensities of elastin I_{Ela} between the
547 crack initiation site and other sites in each specimen. Linear and broken lines show data for
548 $p < 0.05$ and NS, respectively, for comparison between the crack initiation site and other
549 sites within a single specimen. Each mark represents the average within a single specimen

550

551 **Fig. 3** Characteristics of local retardance Ret and slow axis azimuth Azi at crack initiation
552 sites just before rupture. (a and b) Typical (a) retardance and (b) slow axis azimuth
553 distribution in specimen #1. Boxes in images show the crack initiation sites. Bar in (a) = 1
554 mm applies to both images. (c and d) Comparison of (c) mean retardance and (d) slow axis
555 azimuth from the circumferential direction between the crack initiation site and other sites
556 in each specimen. Linear and broken lines show data for $p < 0.05$ and NS, respectively, for
557 comparison between the crack initiation sites and the other sites within a single specimen.
558 Each mark represents the average within a single specimen

559

560 **Fig. 4** Characteristics of collagen fibers in second harmonic generation (SHG) images
561 obtained from crack initiation sites. (a and b) Typical SHG images captured (a) before and

562 (b) after biaxial stretch testing in no load state for specimen #12. Bar in (a) corresponds to
563 250 μm and applies to both images. White arrowheads in (b) show cracks. The center of the
564 red boxes shows the crack initiation point. Color arrows show the same position. (c)
565 Comparison of intensity of SHG images (I_{SHG}) between the crack initiation site and other
566 sites in each specimen. (d) Comparison of standard deviation of the probability distribution
567 of collagen fibers σ between the crack initiation site and other sites in each specimen. Linear
568 and broken lines show data for $p < 0.05$ and NS, respectively, for comparison between the
569 crack initiation site and other sites within a single specimen. Each mark represents the
570 average within a single specimen

571

572 **Fig. 5** Crack direction at crack propagation sites. (a–c) Typical SHG images at crack
573 propagation sites and the probability distributions of collagen fiber orientation along with
574 crack direction. Most cracks propagated in (a) the circumferential direction (0° and $\pm 180^\circ$)
575 and (b) approximately 45° from the circumferential and longitudinal directions and the
576 direction of the cracks corresponded to those of the collagen fibers with high probability
577 although (c) some cracks deviated from this trend. The bar in (c) = 50 μm applies to all
578 images. (d) Histogram of crack angle from the circumferential direction obtained at the
579 crack propagation sites. (e) Angle of a crack $\sim 300 \mu\text{m}$ in length from the circumferential
580 direction at the crack initiation and end sites.

581

582 **Supplementary Figures Captions**

583

584 **Fig. S1** Change in retardance at the intersection of two cellophane tapes placed on a glass
 585 slide at various angles. (a) Illustration of two strips of cellophane tape placed on a glass
 586 slide at angle α . (b) Retardance images of one and two strips of cellophane tape placed in
 587 parallel ($\alpha = 0^\circ$). (c) Retardance images of two strips of cellophane tape placed at various
 588 angles. (d) The relationship between angle α and retardance

589

590 **Fig. S2** Effect of the alignment consistency of collagen fibers on the intensity of SHG
 591 images. (a) A typical image of collagen fibers. (b) Enlarged view of **boxed area indicated**
 592 **with an arrow in** (a). (c) Relationship between intensity at the intersection point of two
 593 collagen fibers $I_{\text{intersection}}$ and the sum of the intensities of the two fibers $I_1 + I_2$. The triangle
 594 plot shows the average intensity of a single fiber, fibers 1 I_1 and 2 I_2 . The broken line
 595 indicates the data when the value in the horizontal axis is the same as that in the vertical
 596 axis. (d) Effect of angle β between two collagen fibers on the intensity ratio I_r at the
 597 intersection point to the sum of the two fibers

598

599 **Fig. S3** Effect of changes in retardance ΔRet between the period just before rupture and the
 600 previous loading step on the crack initiation sites. (a) A typical image of changes in
 601 retardance ΔRet . A black box in the image shows the crack initiation sites. Bar = 1 mm. (b)
 602 Changes in retardance ΔRet at the crack initiation site and at other sites in each specimen

603

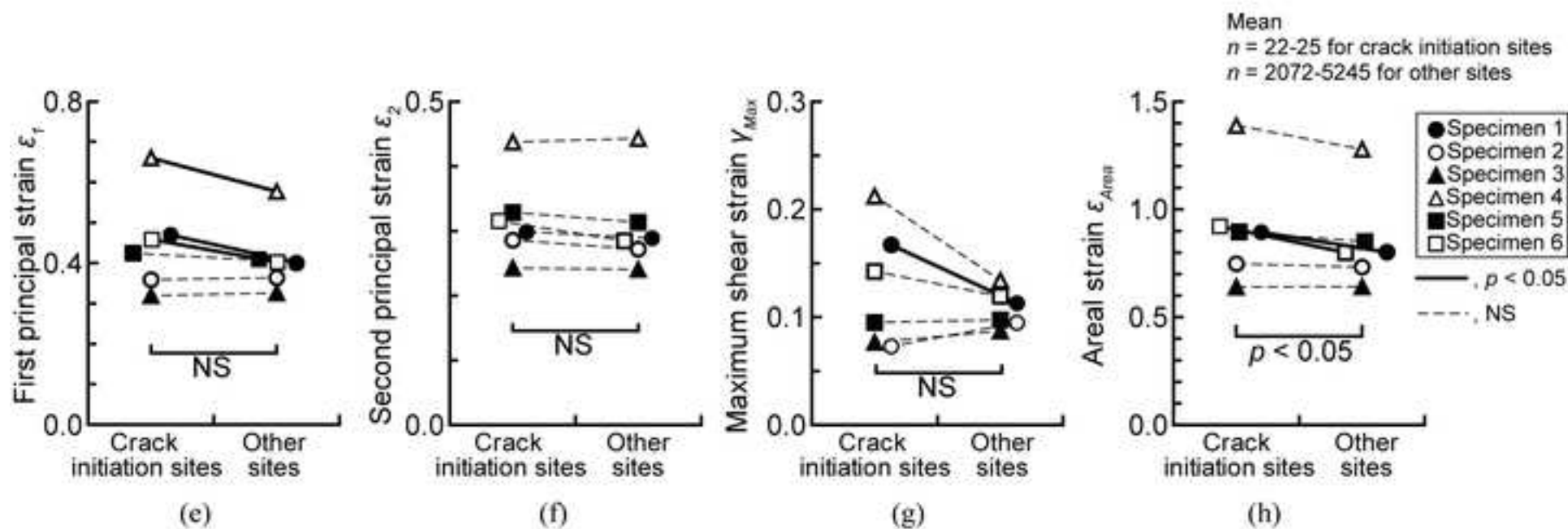
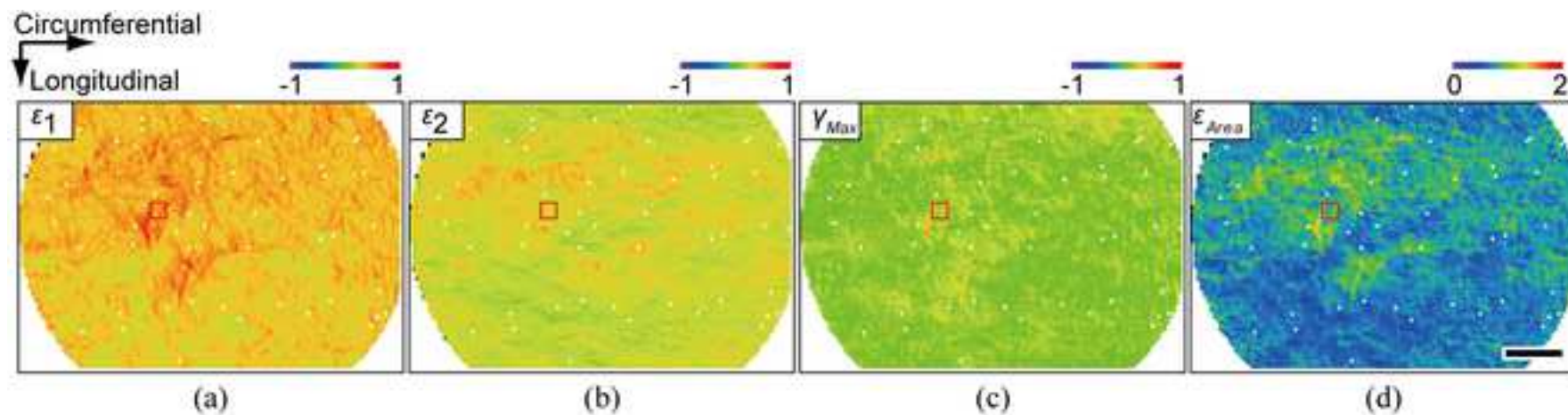
604 **Fig. S4** Typical images of a crack captured at (a) the macroscopic scale and (b) the
 605 microscopic scale. The circle in (a), which shows the circle at the metal frame of the biaxial
 606 stretch tester, corresponds to 10 mm and the bar in (b) = 350 μm

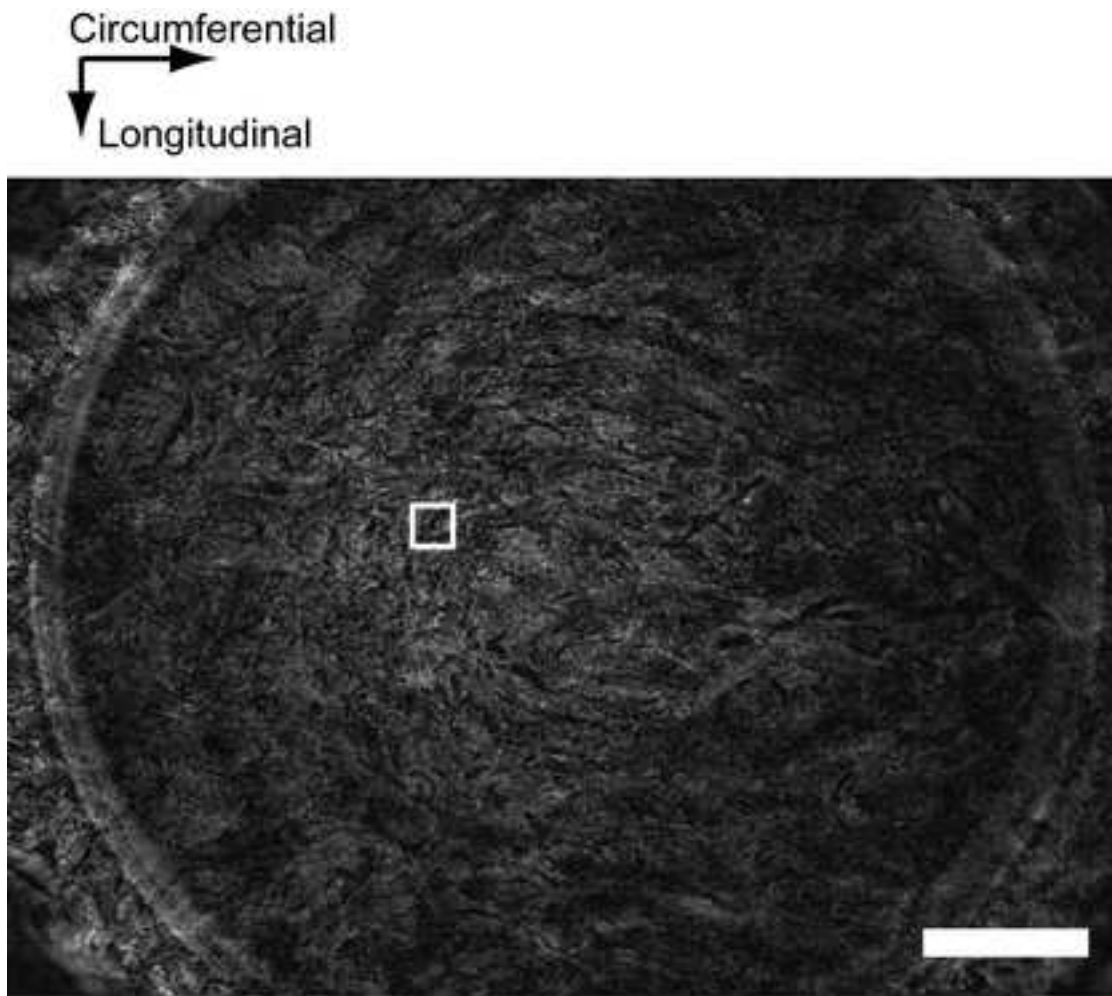
607

608 **Fig. S5** Effect of the analysis size used for the crack initiation sites on retardance between
 609 the crack initiation sites and other sites. The crack initiation sites were changed to (a) 7×7
 610 ($350 \times 350 \mu\text{m}^2$) and (b) 3×3 ($150 \times 150 \mu\text{m}^2$) areas

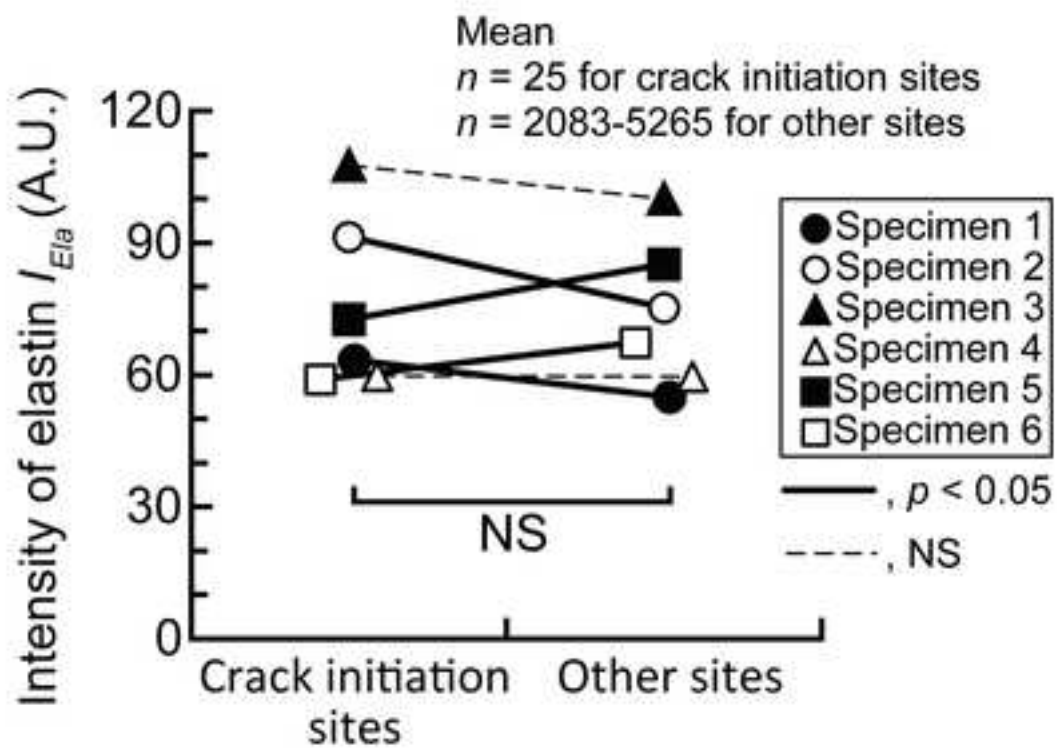
611

612 **Fig. S6** Retardance at the crack initiation site and other sites for thick (150 μm) specimens

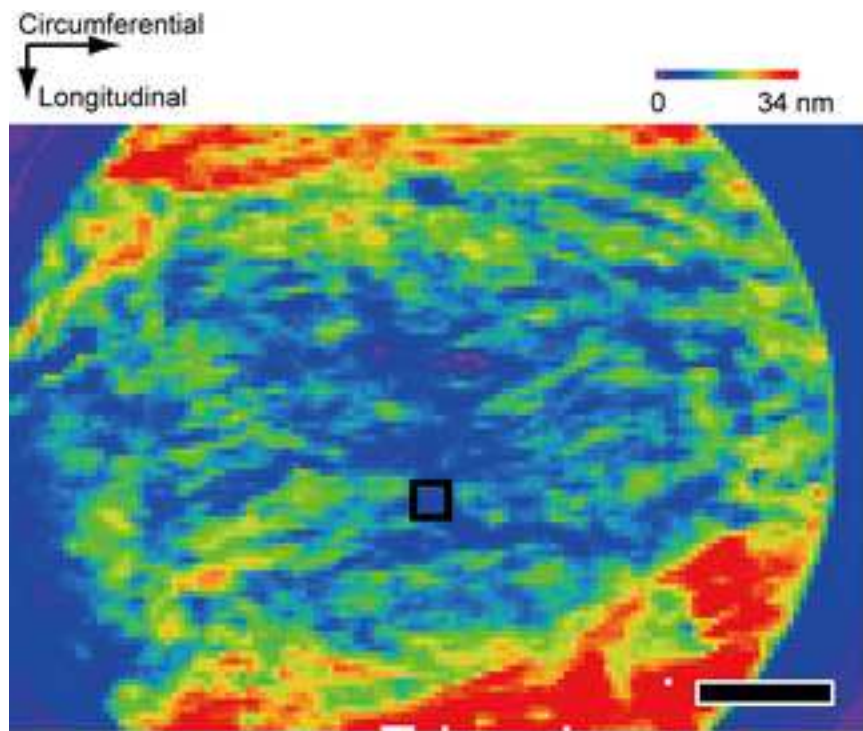




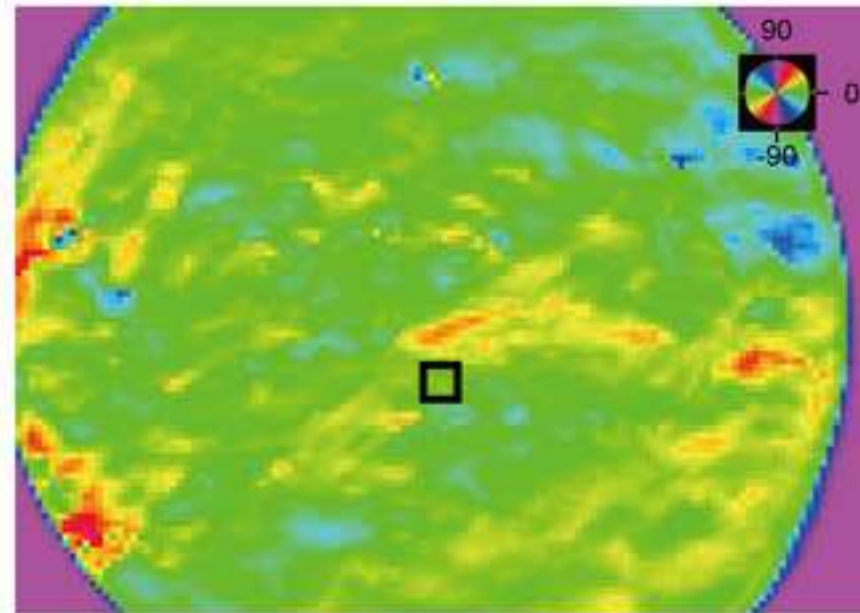
(a)



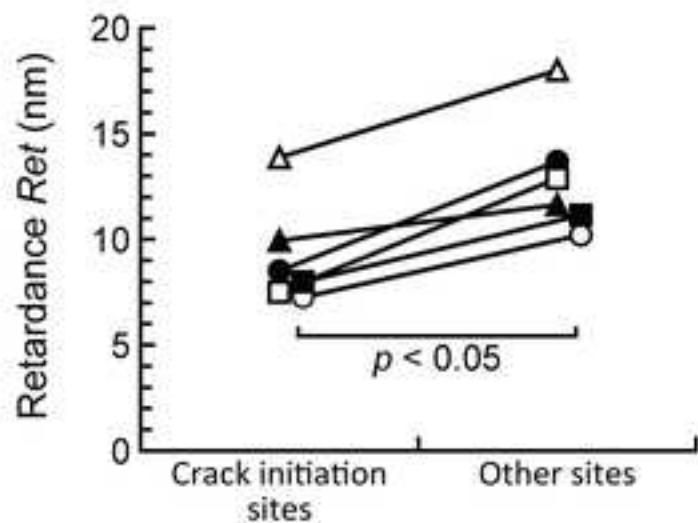
(b)



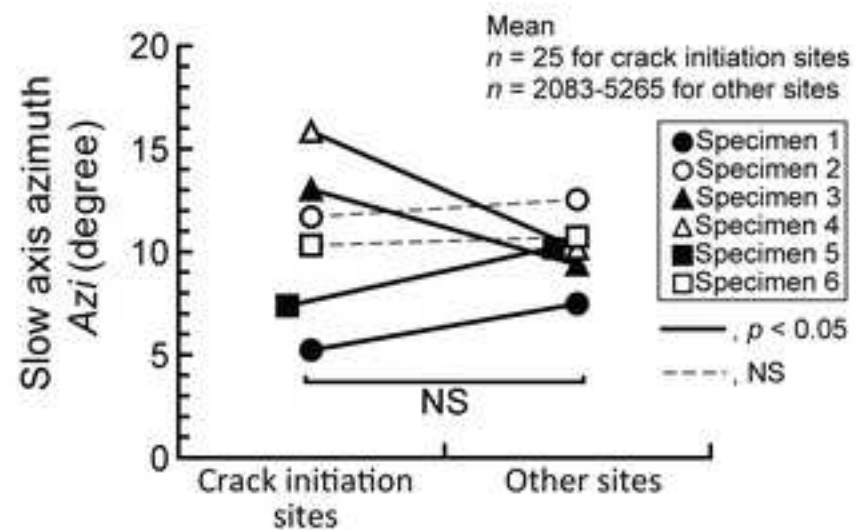
(a)



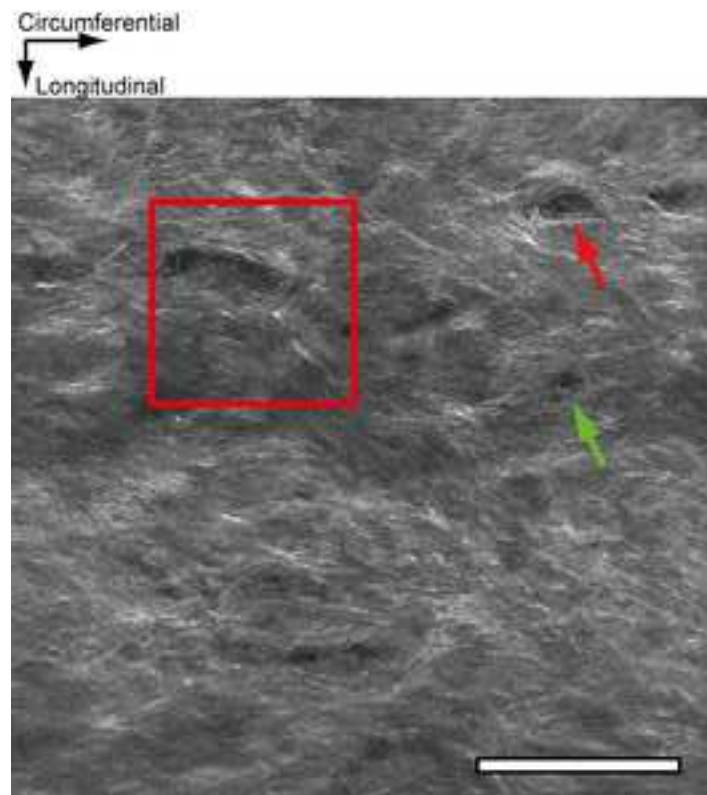
(b)



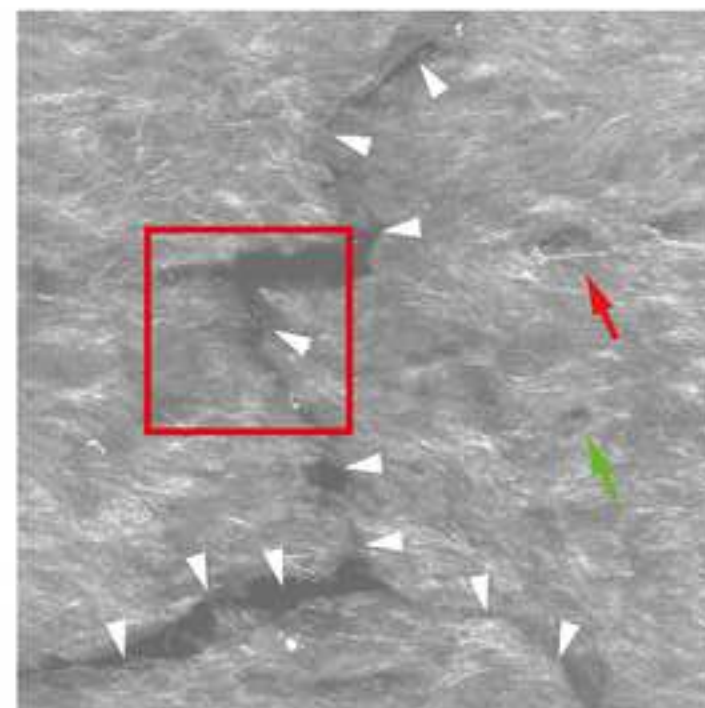
(c)



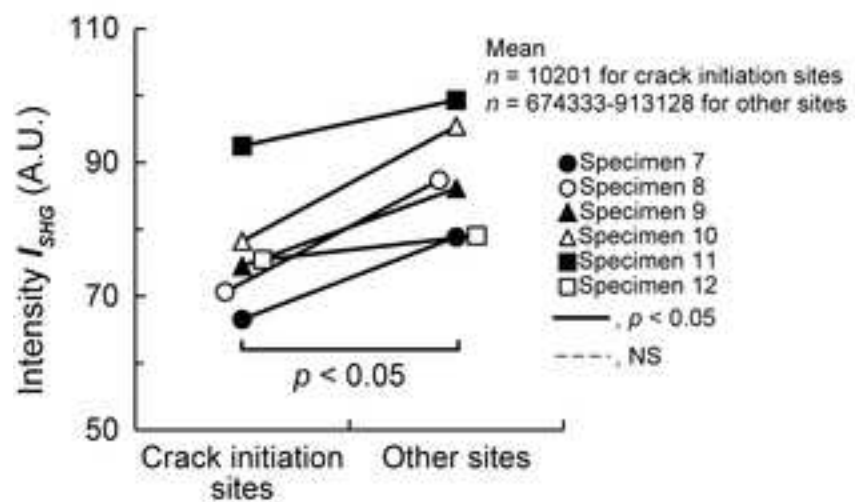
(d)



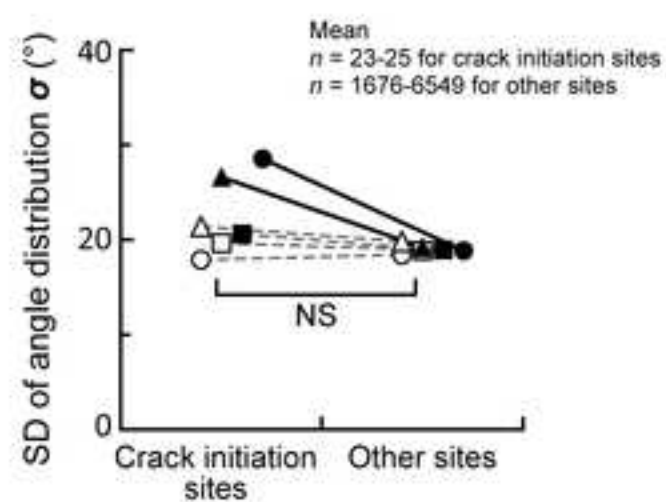
(a)



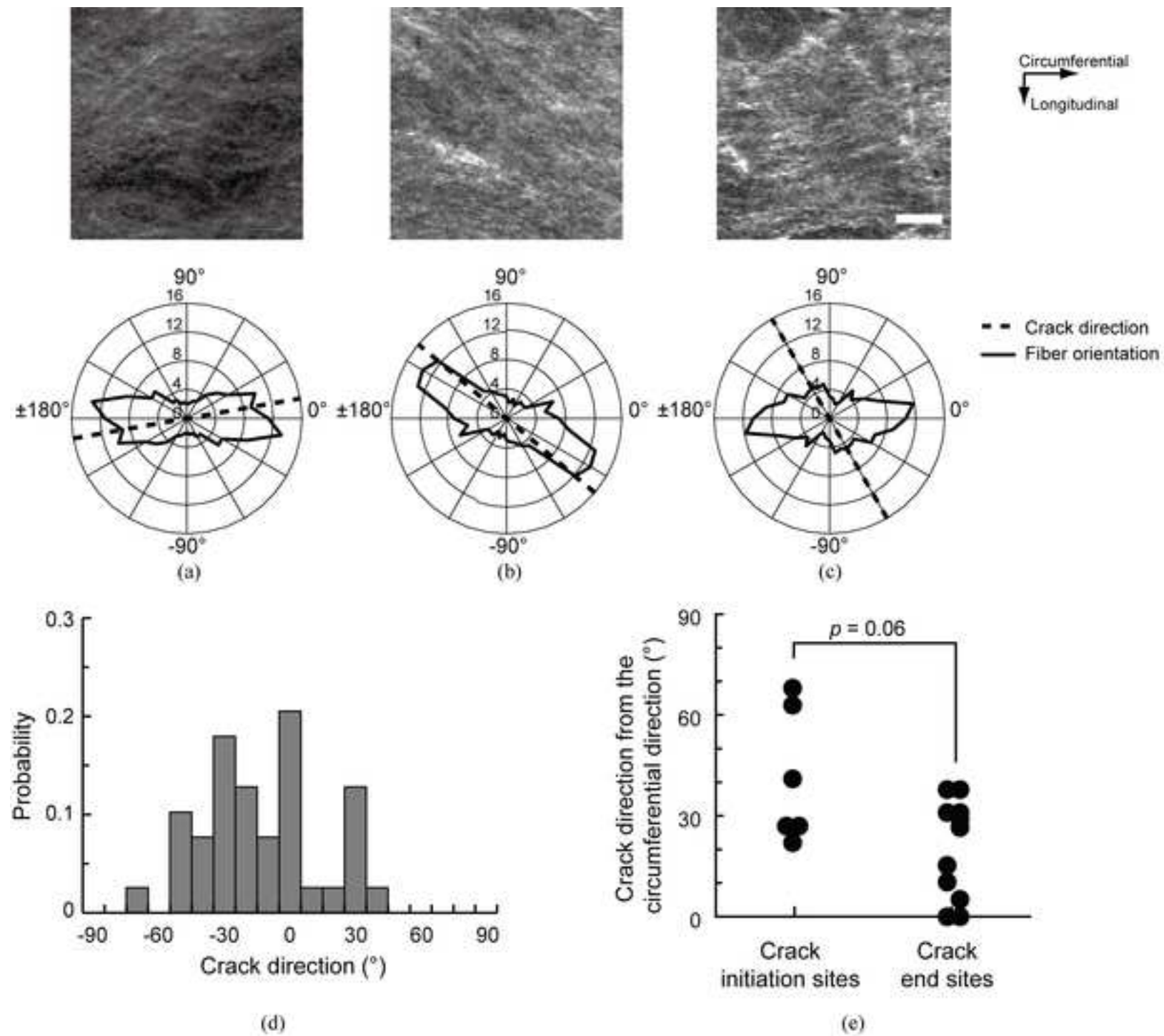
(b)



(c)



(d)



[Click here to view linked References](#)

1

1 **Supplementary Materials (Online Resource)**

2

3 **Title: Local distribution of collagen fibers determines crack initiation site and its**
4 **propagation direction during aortic rupture**

5

6 **Biomechanics and Modeling in Mechanobiology**

7

8 Shukei Sugita and Takeo Matsumoto*, *Nagoya, Japan*

9

10 **Affiliation and address:**

11 Biomechanics Laboratory, Department of Mechanical Engineering, Graduate School of
12 Engineering, Nagoya Institute of Technology, Gokiso-cho, Showa-ku, Nagoya 466-8555,
13 JAPAN

14 *Current: Department of Mechanical Systems Engineering, Graduate School of Engineering,
15 Nagoya University, Furo-cho, Chikusa-ku, Nagoya 464-8603, JAPAN

16

17

18 **To whom correspondence should be addressed:**

19 Shukei Sugita, Ph.D.

20 Department of Mechanical Engineering, Graduate School of Engineering, Nagoya Institute of
21 Technology

22 Gokiso-cho, Showa-ku, Nagoya 466-8555, JAPAN

23 Tel. and Fax: +81 52 735 7125

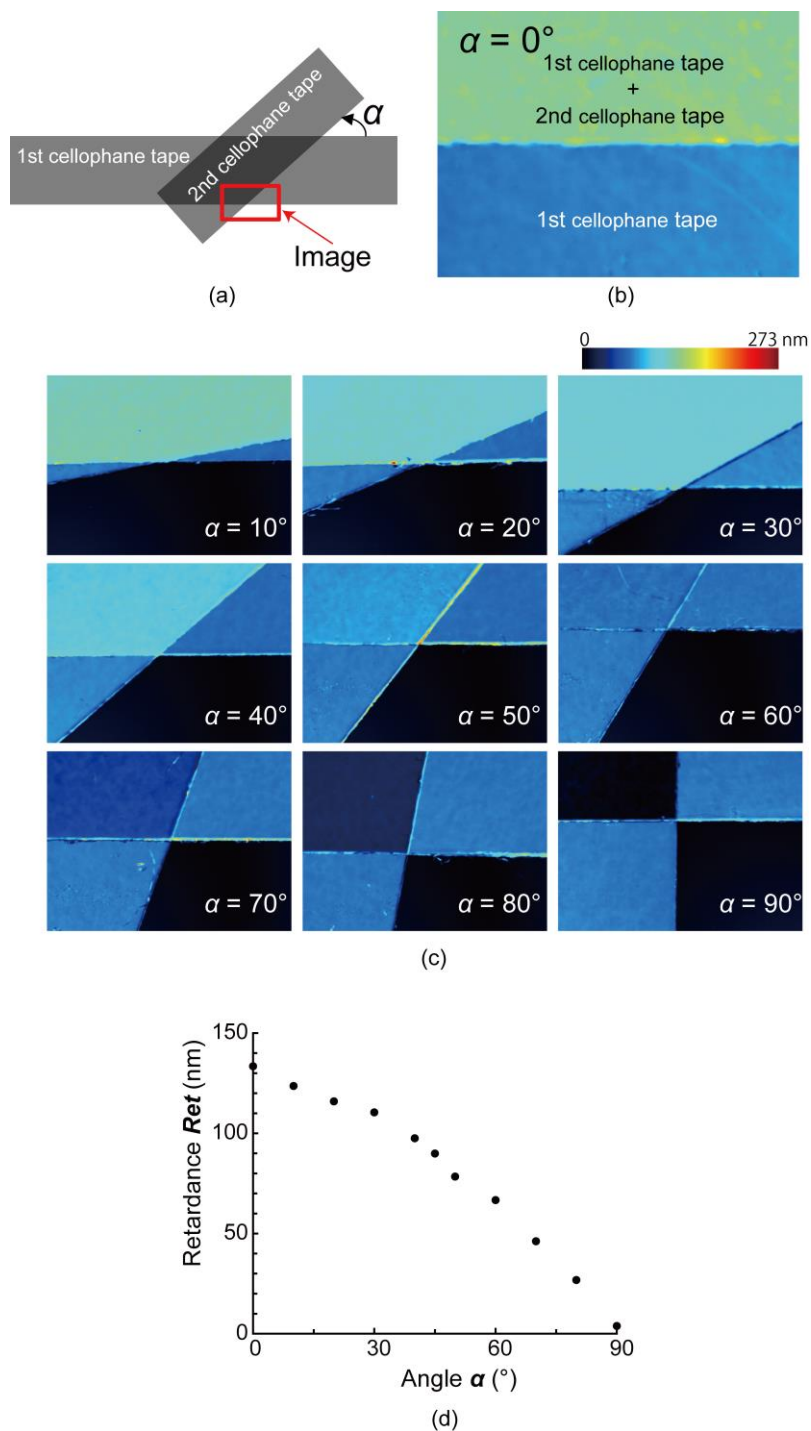
24 E-mail: sugita.shukei@nitech.ac.jp

1 **S1. Effect of alignment consistency of birefringent material on retardance**

2 Retardance is used as an index of the local density of collagen fibers in the aorta (Sugita and
3 Matsumoto 2013). However, it is well known that retardance is also affected by the alignment
4 consistency of birefringent materials, suggesting that retardance decreases when birefringent
5 collagen fibers are not aligned in the same direction. Since we already showed that retardance
6 is proportional to the volume of collagen fibers (Sugita and Matsumoto 2013), we attempted
7 to confirm the effect of the alignment consistency of birefringent materials on retardance using
8 cellophane tape, which is known to be a birefringent material because it is stretched in one
9 direction during the manufacturing process.

10 The alignment consistency of birefringent material was evaluated based on the retardance
11 at the intersection point of two strips of cellophane tape. The two strips of tape were placed on
12 a glass slide with various angles α (Fig. S1a), and their resultant retardance was measured with
13 a birefringent imaging system (Abrio-LS, CRi, Woburn, MA, USA).

14 When the two strips of tape were placed in parallel, retardance in the area covered by the
15 two strips was twice that in the area covered by one strip (Fig. S1b). As the angle between the
16 two strips of tape increased, the retardance in the area covered by the two strips decreased (Fig.
17 S1c and d). When the angle $\alpha = 90^\circ$, the resultant retardance was almost 0 (Fig. S1d). This
18 indicates that retardance is affected by the alignment consistency of birefringent materials.
19 Thus, when the alignment consistency of collagen fibers in the aorta is low, the retardance is
20 not adequate as an index of collagen density.



1

2 **Fig. S1** Change in retardance at the intersection of two cellophane tapes placed on a glass slide
 3 at various angles. (a) Illustration of two strips of cellophane tape placed on a glass slide at angle
 4 α . (b) Retardance images of one and two strips of cellophane tape placed in parallel ($\alpha = 0^\circ$).
 5 (c) Retardance images of two strips of cellophane tape placed at various angles. (d) The
 6 relationship between angle α and retardance

1 **S2. Effect of alignment consistency of collagen fibers on SHG intensity**

2 To evaluate collagen density with no effect from the alignment consistency of collagen
3 fibers, second harmonic generation (SHG) signals were employed in this study. To evaluate the
4 effect of the alignment consistency of collagen fibers on the SHG signal, the intensity at the
5 intersection point of two collagen fibers was investigated.

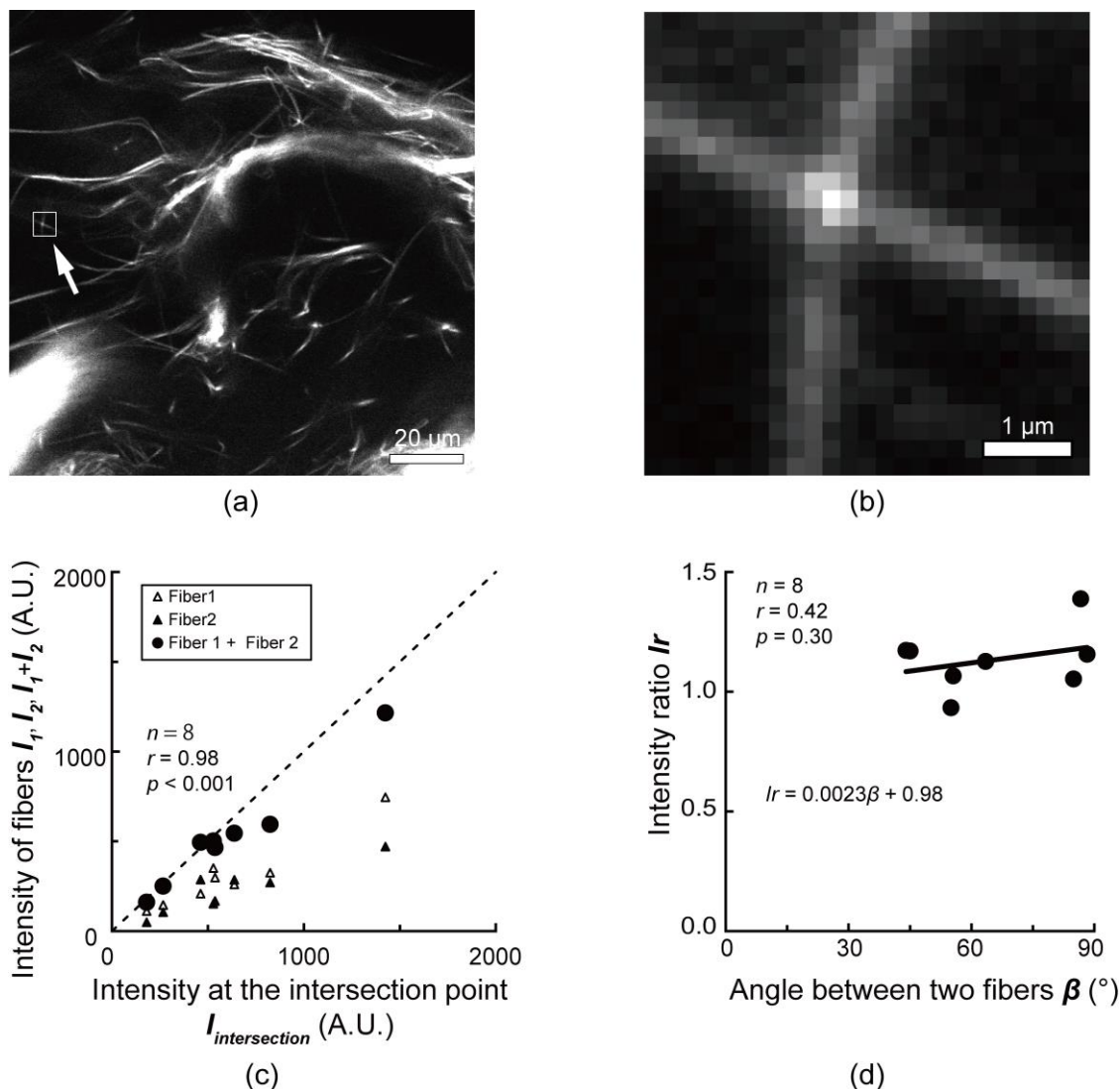
6 Collagen fibers obtained from mouse tail tendons were mounted on a glass slide and
7 observed under the SHG microscope (FV1200MPE, Olympus) as stated in the *Second*
8 *harmonic generation (SHG) light observation* subsection in the Materials and methods section.
9 Animal experiments were approved by the institutional review board for animal care at the
10 Nagoya Institute of Technology. Image analysis was performed with image analysis software
11 (ImageJ, National Institutes of Health). In the obtained SHG image (Fig. S2a), areas showing
12 the intersection of two collagen fibers in a confocal plane were selected (Fig. S2b). Intensity at
13 the intersection point of two collagen fibers $I_{\text{intersection}}$ and the average intensity along each
14 collagen fiber I_1 , I_2 were measured, and the results were compensated by subtracting the
15 background intensity around the fibers. The sum of the average intensities of the two collagen
16 fibers $I_1 + I_2$ was then compared with the intensity at the intersection point $I_{\text{intersection}}$, as the
17 intensity ratio I_r , to exclude the influence of the width of the collagen fibers as follows:

$$18 \quad I_r = \frac{I_1 + I_2}{I_{\text{intersection}}}. \quad (\text{S1})$$

19 The ratio I_r was then plotted against the angle β to evaluate the effect of the angle β between
20 two fibers on SHG intensity.

21 Figure S2c shows the relationship between intensity at the intersection point of two collagen
22 fibers and the sum of the intensities of the two fibers (fiber 1 + fiber 2). Intensity at the
23 intersection point was almost the same as the sum of the intensities of two fibers. This indicates
24 that SHG intensities can be used to quantify the density of collagen fibers. Figure S2d shows
25 the relationship between the angle β of two collagen fibers and the intensity ratio I_r at the
26 intersection point to the sum of the two fibers. The correlation was insignificant ($p = 0.30$), and
27 the intensity ratio I_r was not significantly affected by angle β , indicating that the alignment
28 consistency of the collagen fibers does not affect the intensity of the SHG image of collagen

1 fibers.



2

3 **Fig. S2** Effect of the alignment consistency of collagen fibers on the intensity of SHG images.

4 (a) A typical image of collagen fibers. (b) Enlarged view of boxed area indicated with an arrow

5 in (a). (c) Relationship between intensity at the intersection point of two collagen fibers

6 $I_{\text{intersection}}$ and the sum of the intensities of the two fibers $I_1 + I_2$. The triangle plot shows the

7 average intensity of a single fiber, fibers 1 I_1 and 2 I_2 . The broken line indicates the data when

8 the value in the horizontal axis is the same as that in the vertical axis. (d) Effect of angle β

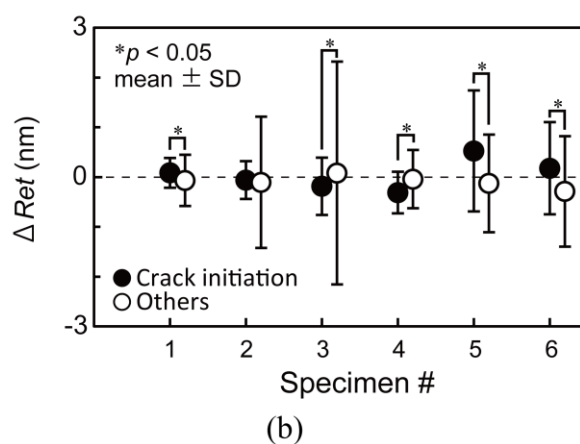
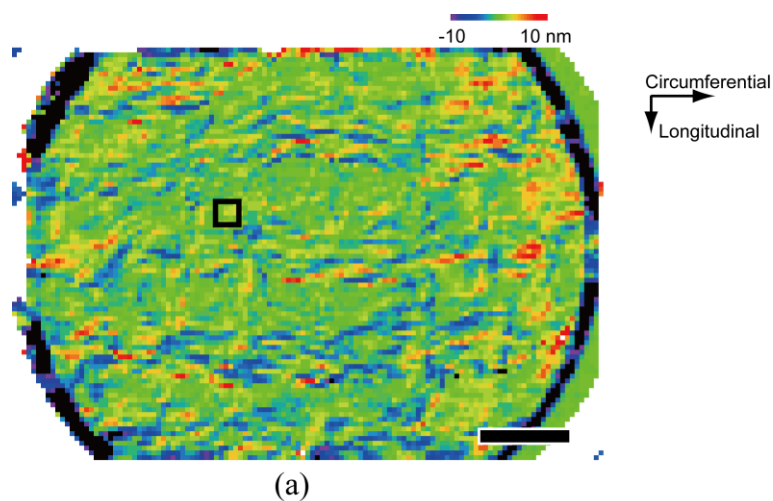
9 between two collagen fibers on the intensity ratio I_r at the intersection point to the sum of the

10 two fibers

1 **S3. Characteristics of changes in retardance between the period just before rupture and**
 2 **the previous loading step at the crack initiation sites**

3 The effect of changes in retardance on the crack initiation sites was studied because the
 4 network of collagen fibers at the crack initiation sites might change just before rupture. For this
 5 purpose, we calculated the changes in retardance ΔRet by subtracting the retardance just before
 6 rupture from the retardance at the previous loading step at each local area.

7 Figure S3a shows a typical image of changes in retardance ΔRet . Although the changes in
 8 retardance ΔRet seem to be heterogeneously distributed, statistical analysis shows no clear
 9 tendency; changes in retardance ΔRet were significantly higher at the crack initiation site in
 10 some specimens (#1, #5, and #6) and lower in other specimens (#3 and #4; Fig. S3b). These
 11 results indicate that the changes in retardance ΔRet are not related to the crack initiation.



12

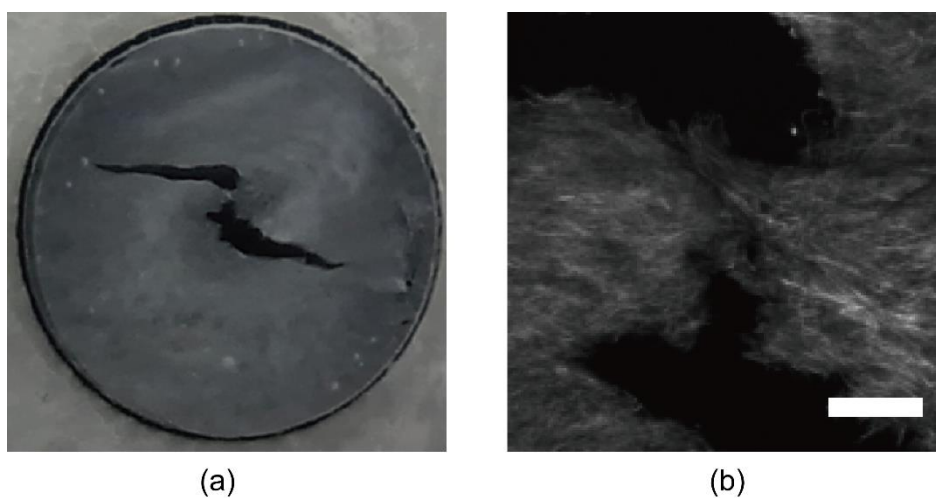
13 **Fig. S3** Effect of changes in retardance ΔRet between the period just before rupture and the
 14 previous loading step on the crack initiation sites. (a) A typical image of changes in retardance

- 1 ΔRet . A black box in the image shows the crack initiation sites. Bar = 1 mm. (b) Changes in
- 2 retardance ΔRet at the crack initiation site and at other sites in each specimen

1 **S4. Crack direction observed at the microscopic and macroscopic scales**

2 Figure S4a and b show typical specimen images captured with a digital camera and SHG
3 microscope, respectively, after the biaxial tensile test. Although the crack around the crack
4 initiation sites appears to run in the longitudinal direction, cracks far from the crack initiation
5 sites run in the circumferential direction in the macroscopic image. Microscopically, this crack
6 runs in a zigzag direction around the crack initiation site as the crack seems to run along the
7 collagen fibers (Fig. S4b).

8



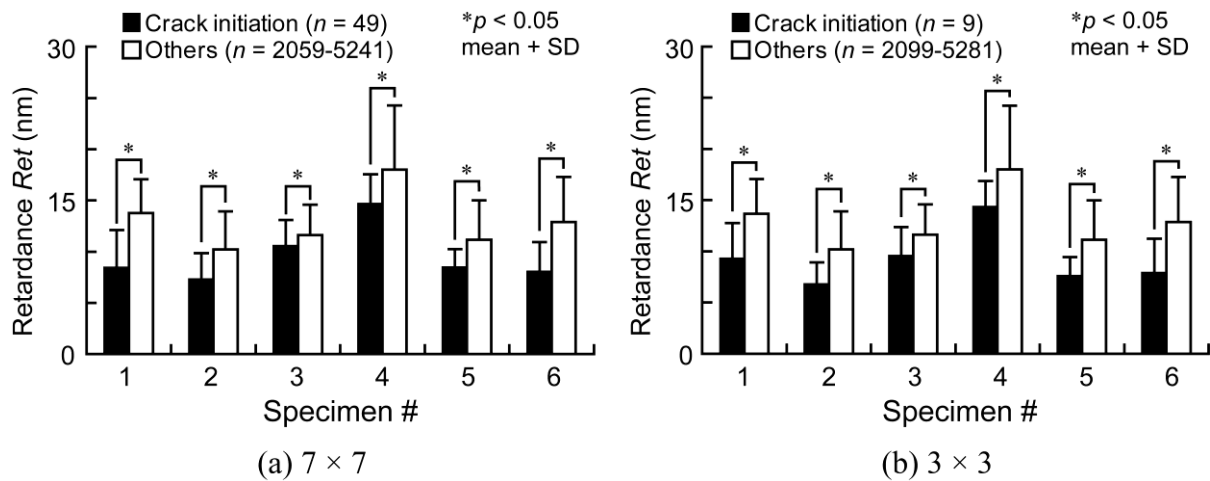
10 **Fig. S4** Typical images of a crack captured at (a) the macroscopic scale and (b) the microscopic
11 scale. The circle in (a), which shows the circle at the metal frame of the biaxial stretch tester,
12 corresponds to 10 mm and the bar in (b) = 350 μm

1 S5. Evaluation of the analysis size of the crack initiation sites

2 The crack initiation sites were identified as 5×5 areas of 10×10 pixels ($50 \times 50 \mu\text{m}^2$), that
 3 is, $250 \times 250 \mu\text{m}^2$. To evaluate the analysis size used for the crack initiation sites, the size was
 4 increased to 7×7 ($350 \times 350 \mu\text{m}^2$) and decreased to 3×3 ($150 \times 150 \mu\text{m}^2$).

5 Fig. S5a and b show the comparison between the retardance at 7×7 and 3×3 regions for
 6 the crack initiation sites, respectively, and retardance at other sites within a single specimen.
 7 Even though the size of the crack initiation sites was changed, the retardance at the crack
 8 initiation sites remained significantly lower than the values at other sites for all specimens.

9



10

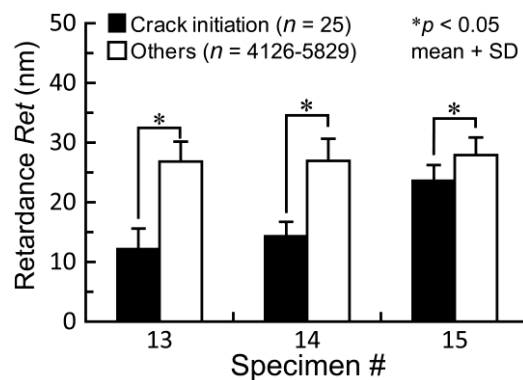
11 **Fig. S5** Effect of the analysis size used for the crack initiation sites on retardance between the
 12 crack initiation sites and other sites. The crack initiation sites were changed to (a) 7×7 ($350 \times$
 13 $350 \mu\text{m}^2$) and (b) 3×3 ($150 \times 150 \mu\text{m}^2$) areas

1 **S6. The effect of specimen slice thickness**

2 To modify the shape of the specimen that enabled us to observe the crack initiation sites
 3 during biaxial stretching and to observe SHG light from the specimens, specimens were sliced
 4 into 50- μm sections, which might affect collagen structure around the surface area. To evaluate
 5 the slice thickness of the specimens, we performed a biaxial stretch test for thick specimens,
 6 which were sliced into 150- μm sections, and obtained the retardance distribution ($n = 3$).

7 Figure S6 shows the retardance at both the crack initiation site and other sites in thick
 8 specimens. Retardance was significantly lower at the crack initiation sites than at other sites
 9 within the same specimen for all three specimens (Fig. S6). This indicates that the effect of
 10 slicing the specimen would have been very small.

11



12

13 **Fig. S6** Retardance at the crack initiation site and other sites for thick (150 μm) specimens

1 **Reference**

- 2 Sugita S, Matsumoto T (2013) Quantitative measurement of the distribution and alignment of
3 collagen fibers in unfixed aortic tissues. *J Biomech* 46:1403-1407
4 doi:10.1016/j.jbiomech.2013.02.003